IEICE TRANSACTIONS

on Electronics

VOL. E99-C NO. 1
JANUARY 2016



A PUBLICATION OF THE ELECTRONICS SOCIETY

The Institute of Electronics, Information and Communication Engineers
Kikai-Shinko-Kaikan Bldg., 5-8, Shibakoen 3 chome, Minato-ku, TOKYO, 105-0011 JAPAN

IEICE TRANS. ELECTRON., VOL.E99–C, NO.1 JANUARY 2016

BRIEF PAPER *Special Section on Recent Progress in Electromagnetic Theory and Its Application*

# Efficient Scattering Analysis of Arbitrarily Shaped Local Defect in Diffraction Grating

**Jun-ichiro SUGISAKA**[†a)], **Takashi YASUI**[†], ***and*** **Koichi HIRAYAMA**[†], ***Members***

**SUMMARY** We propose an algorithm for the scattering analyses of gratings with various local defects based on the difference-field boundary-element method (DFBEM). In the algorithm, the defect in the grating is partitioned, and the DFBEM is sequentially applied for each defect section. We validate the proposed algorithm by demonstrating its flexibility for various defect topologies for a locally deformed grating.

***key words:*** *diffraction grating, boundary-element method, defect, scattering, numerical analysis*

## 1. Introduction

Local defects in diffractive optical elements (DOEs) with periodic groove patterns affect the optical properties. When analyzing and detecting the defects in such DOEs, numerical simulation is an essential process. The analyses of defective gratings require considerable calculation resources. In general, the DOEs have wavelength-order grooves, and incident waves illuminate over a large spatial area. Thus, we must discretize the electromagnetic (vectorial) field distribution over a large spatial area with an interval that is less than the wavelength. Bloch's boundary conditions, which reduce the analysis area to one period, cannot be applied because the periodicity in the DOE disappears owing to the defects. So far, defective DOEs have been analyzed by using a finite-difference time-domain (FDTD) method [1], rigorous coupled-wave analysis (RCWA) [2], and finite element method (FEM) [3]. Several unique methods for the analyses of defective grating structures have also been proposed [4], [5].

In our previous work, we have developed a difference-field boundary-element method (DFBEM) [6]. The field for the defective DOE (called the total field) is decomposed into a base field (a field for a nondefective structure) and a difference field. The base-field component is easily found by solving a wave equation with Bloch's boundary conditions. On the other hand, the difference-field component is found by solving boundary-integral equations (BIEs). So far, we have derived BIEs for three types of defects: (I) a projection defect (e.g., the air region outside of the grating is partially replaced by the substrate material), (II) a crack defect (e.g., the substrate region inside of the grating is partially replaced by air), and (III) a buried-pillar defect. However, the BIEs depend on the defect topology; thus, we must derive BIEs for other defect topologies. It is impractical to derive BIEs every time when we analyze the various defective DOEs.

In this paper, we propose another approach for the analyses of various defect types; the defect is partitioned into sections that belong to either defect-type (I), (II), or (III) and sequentially apply the DFBEM to each defect section. We describe the calculation method in the following section by showing an analysis of a locally deformed grating.

## 2. Numerical Method and Demonstration

The cross sections of the original (periodic) grating and the locally deformed grating are shown in Figs. 1 (a) and 1 (b), respectively. The cross section is in the $x - y$ plane, and the structure along $z$ axis is uniform. The refractive indices inside and outside the grating are 1.5 and 1.0, respectively. The grating period $T$, groove depth, and groove width were set to $3.5\lambda$, $0.3T$, and $0.5T$, respectively. The parameter $\lambda$ is the wavelength of the incident wave. The incident wave is a plane wave of $p$-polarization propagating in the direction of $-45°$.

We label the integral paths and region around the defect as shown in Fig. 2 (a). $C_{11}$ and $C_{12}$ are the surface of the original grating, and $C_{21}$ and $C_{22}$ are the surface of the deformed grating. The filled circles indicate the boundary-element nodes. The node positions on $C_{21}$ and $C_{22}$ are listed in Table 1. These boundaries partition the defect into two sections ($S_{31}$ and $S_{32}$). In the following process, these two defect sections are sequentially added to the periodic grating, and the field distribution is updated by using the DFBEM.

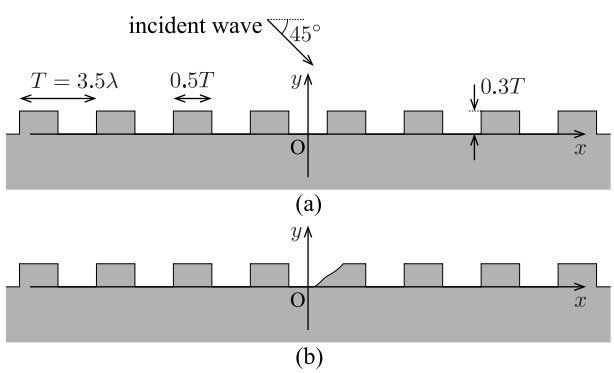


**Fig. 1** Cross sections of (a) the original periodic grating and (b) the locally deformed grating.

Manuscript received March 30, 2015.
Manuscript revised July 30, 2015.

[†]The authors are with Kitami Institute of Technology, Kitami-shi, 090–8507 Japan.
a) E-mail: sugisaka@mail.kitami-it.ac.jp

DOI: 10.1587/transele.E99.C.76

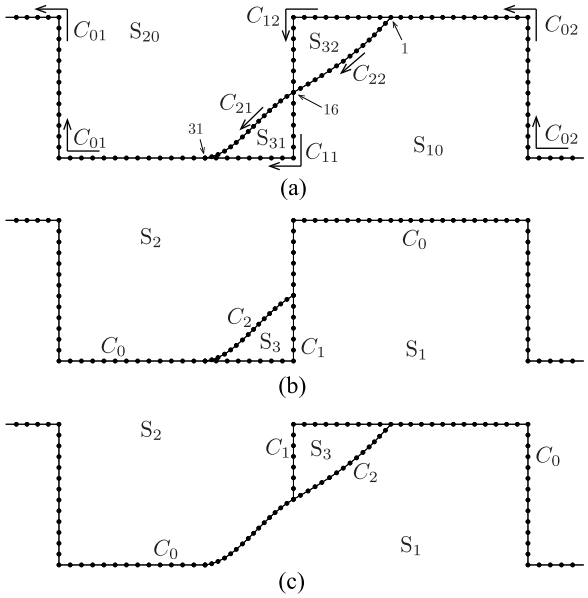


**Fig. 2** (a) Integral paths of the deformed grating discretized by boundary elements. The numbers 1, 16, and 31 indicate the node number listed in Table 1. (b) Integral paths for adding the $S_{31}$ defect section. (c) Integral paths for adding the $S_{32}$ defect section.

**Table 1** Positions of the element nodes on $C_{21}$ and $C_{22}$

| node | $x/T$ | $y/T$ | node | $x/T$ | $y/T$ |
|---|---|---|---|---|---|
| 1 | 0.4577 | 0.3000 | 17 | 0.2361 | 0.1314 |
| 2 | 0.4461 | 0.2871 | 18 | 0.2229 | 0.1216 |
| 3 | 0.4338 | 0.2745 | 19 | 0.2108 | 0.1116 |
| 4 | 0.4224 | 0.2624 | 20 | 0.1992 | 0.1010 |
| 5 | 0.4113 | 0.2515 | 21 | 0.1876 | 0.08995 |
| 6 | 0.3982 | 0.2399 | 22 | 0.1760 | 0.07861 |
| 7 | 0.3845 | 0.2284 | 23 | 0.1649 | 0.06753 |
| 8 | 0.3706 | 0.2173 | 24 | 0.1536 | 0.05644 |
| 9 | 0.3562 | 0.2064 | 25 | 0.1412 | 0.04485 |
| 10 | 0.3420 | 0.1964 | 26 | 0.1281 | 0.03325 |
| 11 | 0.3268 | 0.1861 | 27 | 0.1162 | 0.02371 |
| 12 | 0.3106 | 0.1758 | 28 | 0.1031 | 0.01469 |
| 13 | 0.2961 | 0.1668 | 29 | 0.08918 | 0.007474 |
| 14 | 0.2812 | 0.1577 | 30 | 0.07577 | 0.002577 |
| 15 | 0.2649 | 0.1485 | 31 | 0.06160 | 0.0 |
| 16 | 0.2500 | 0.1399 | | | |

In preparation, we calculated the base field, i.e. the field for the original rectangular grating in Fig. 1 (a). Many numerical methods such as the FDTD method, RCWA, FEM, and BEM provide the field for the periodic structure. We selected a method using a BEM with Bloch's boundary condition [7]. The grating surface was discretized by boundary elements (constant elements) with element lengths less than $\lambda/12$. We denote the field (the $z$ component of the magnetic field) distributions in $S_1 \equiv S_{10} \cup S_{32}$ and $S_2 \equiv S_{20} \cup S_{31}$ as $f_1^{(1)}$ and $f_2^{(1)}$, respectively. Fields of the grating at arbitrary points, for example, distribution around the grating surface and diffracted waves (far fields) correspond to $f_1^{(1)}$ and $f_2^{(1)}$. At least $f_1^{(1)}$ and $\partial f_1^{(1)}/\partial n$ ($n$ represents the outward normal direction on the boundary) on $C_{11}$ and $C_{12}$, $f_1^{(1)}$ on $C_{22}$, and $f_2^{(1)}$ on $C_{21}$ must be obtained. These values appear in the following BIEs as constant terms.

First, we added the defect section $S_{31}$ to the periodic grating. The defect section $S_{31}$ corresponds to Pattern (I), because the air region in $S_{31}$ is replaced by the substrate material. In the computation for Pattern (I) defect, we define three regions $S_1$ (inside of the grating), $S_2$ (outside of the grating), and $S_3$ (inside of the defect). We also denote the fields in $S_1$, $S_2$, and $S_3$ as $f_1^{(1)} + \Delta f_1^{(1)}$, $f_2^{(1)} + \Delta f_2^{(1)}$, and $f_3^{(1)}$. BIEs for Pattern (I) consist of three integral paths; $C_0$, $C_1$, and $C_2$. $C_0$, $C_1$, and $C_2$ are defined as the boundary between $S_1$ and $S_2$, the boundary between $S_1$ and $S_3$, and the boundary between $S_2$ and $S_3$. As shown in Fig. 2 (b), those regions and paths are defined as follows:

$$S_1 = S_{10} \cup S_{32}, \quad S_2 = S_{20}, \quad S_3 = S_{31},$$
$$C_0 = C_{01} \cup C_{12} \cup C_{02}, \quad C_1 = C_{11}, \quad C_2 = C_{21}.$$

We truncated the infinitely long path $C_0$ at $x = \pm 5.25T$, because the integrand in the path integral on $C_0$ converges to zero at far distance.

The BIEs for Pattern (I) defect are written in Eqs. (14), (15), and (20)–(23) in [6]. The constant terms of the BIEs are given by the base field $f_1^{(1)}$ and $\partial f_1^{(1)}/\partial n$ on $C_1$ and $f_2^{(1)}$ on $C_2$. The BIEs are numerically solved as a set of simultaneous equations. By solving the BIEs, we obtain $\Delta f_1^{(1)}$ on $C_0$, $f_3^{(1)}$ on $C_1$, and $f_3^{(1)}$ on $C_2$ and their derivatives with respct to $n$. The fields $\Delta f_1^{(1)}$, $\Delta f_2^{(1)}$, and $f_3^{(1)}$ at other positions are given by the integral expressions for Pattern (I) (Eqs. (24)–(26) in [6]), which are defined by the path integrals of the solution of the BIEs and free-space Green's functions on $C_0$, $C_1$, and $C_2$. For the following DFBEM process, we must compute $f_1^{(1)} + \Delta f_1^{(1)}$ and $\partial(f_1^{(1)} + \Delta f_1^{(1)})/\partial n$ on $C_{12}$ and $f_1^{(1)} + \Delta f_1^{(1)}$ on $C_{22}$. The difference-field components $\Delta f_1^{(1)}$ and $\partial \Delta f_1^{(1)}/\partial n$ on $C_{12}$, which is a part of $C_0$, are included in the solution of the BIEs. The difference-field component $\Delta f_1^{(1)}$ on $C_{22}$ is given by the integral expressions.

Next, we regarded the total field as a new base field. Then, we added the remaining defect section $S_{32}$. This defect topology corresponds to Pattern (II), because $S_{32}$ is a part of the substrate region and is replaced by air. The regions $S_1$, $S_2$, and $S_3$ are defined similarly to those for Pattern (I). We denote the fields in $S_1$, $S_2$, and $S_3$ as $f_1^{(2)} + \Delta f_1^{(2)}$, $f_2^{(2)} + \Delta f_2^{(2)}$, and $f_3^{(2)}$. $f_1^{(2)}$ and $f_2^{(2)}$ are the new base-field components, which are defined by

$$f_1^{(2)} = f_1^{(1)} + \Delta f_1^{(1)} \quad \text{in} \quad S_{10}, \tag{1}$$
$$f_1^{(2)} = f_3^{(1)} \quad \text{in} \quad S_{31}, \tag{2}$$
$$f_2^{(2)} = f_2^{(1)} + \Delta f_2^{(1)}. \tag{3}$$

The BIEs for Pattern (II) consist of path integrals on three boundaries; $C_0$ (between $S_1$ and $S_2$), $C_1$ (between $S_2$ and $S_3$), and $C_2$ (between $S_1$ and $S_3$). As sketched in Fig. 2 (c), those regions and paths were defined by

$$C_0 = C_{01} \cup C_{21} \cup C_{02}, \quad C_1 = C_{12}, \quad C_2 = C_{22},$$
$$S_1 = S_{10} \cup S_{31}, \quad S_2 = S_{20}, \quad S_3 = S_{32}.$$

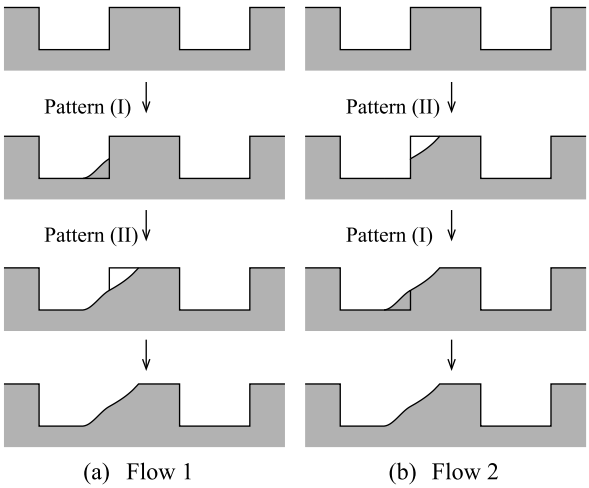


**Fig. 3** Two sequential procedures for obtaining a deformed-groove structure: (a) Flow 1 and (b) Flow 2. These procedures differ in the order of adding two defect sections.

We truncated the infinitely long path $C_0$ at $x = \pm 5.25T$.

The BIEs for Pattern (II) defect is written in Eqs. (31), (32), and (37)–(40) in [6]. The constant terms also consist of $f_1^{(2)}$ and $\partial f_1^{(2)}/\partial n$ on $C_1$ and $f_1^{(2)}$ on $C_2$. These values are given by the preparation process and the previous DFBEM process. The BIEs give the solution $\Delta f_1^{(2)}$ on $C_0$, $f_3^{(2)}$ on $C_1$, $\Delta f_3^{(2)}$ on $C_2$, including their derivatives with respect to $n$. The fields at other points are given by the integral expressions for Pattern (II) (Eqs. (41)–(43) in [6]). The obtained total field corresponds to the field for the deformed-groove grating [Fig. 1 (b)].

In the above process, the defect sections were added to the periodic grating by Flow 1 in Fig. 3 (a). Even if the two defect sections are added in a different order (Flow 2), as shown in Fig. 3 (b), we must obtain identical results. We next calculated the field distribution by Flow 2. In Flow 2, we first added the defect section $S_{32}$ to the periodic grating and solved the BIEs for Pattern (II) with the following definition:

$$C_0 = C_{01} \cup C_{11} \cup C_{02}, \quad C_1 = C_{12}, \quad C_2 = C_{22},$$
$$S_1 = S_{10}, \quad S_2 = S_{20} \cup S_{31}, \quad S_3 = S_{32}.$$

Then, we added the defect section $S_{31}$ and solved the BIEs for Pattern (I) with the following definition:

$$C_0 = C_{01} \cup C_{22} \cup C_{02}, \quad C_1 = C_{11}, \quad C_2 = C_{21},$$
$$S_1 = S_{10}, \quad S_2 = S_{20} \cup S_{32}, \quad S_3 = S_{31}.$$

The resultant field distributions obtained by Flow 1 and Flow 2 are shown in Figs. 4 (a) and 4 (b), respectively. These field distributions are normalized by the amplitude of the incident wave. The shapes of the wavefronts for Flow 1 and Flow 2 agree well overall. In Fig. 4 (c), we plot the error between the total fields of Flow 1 and Flow 2 (absolute value of the difference). The error is at most $1.160 \times 10^{-2}$ (0.4468% of the maximum value of the total field); the field distributions obtained by Flow 1 and Flow 2 are in good agreement. This error is due to the error in the integrands (the fields at the boundaries) of the integral expressions. For a smaller error, more accurate expressions of the fields at the boundaries are necessary by using finer (shorter) or higher-order elements. The convergence of the error between Flow 1 and Flow 2 is shown in Fig. 5. The error is the difference in the total fields for Flow 1 and Flow 2 at the position $(x, y) = (0.16T, 0.033T)$. This position belongs to $S_{31}$, where we observed larger error than that in the other regions in Fig. 4 (c). The lateral axis $N$ indicates that the lengths of the boundary elements were set so as to be less than $\lambda/N$. The result shows that the error between Flow 1 and Flow 2 exponentially decreases as the element length $\lambda/N$ becomes shorter.

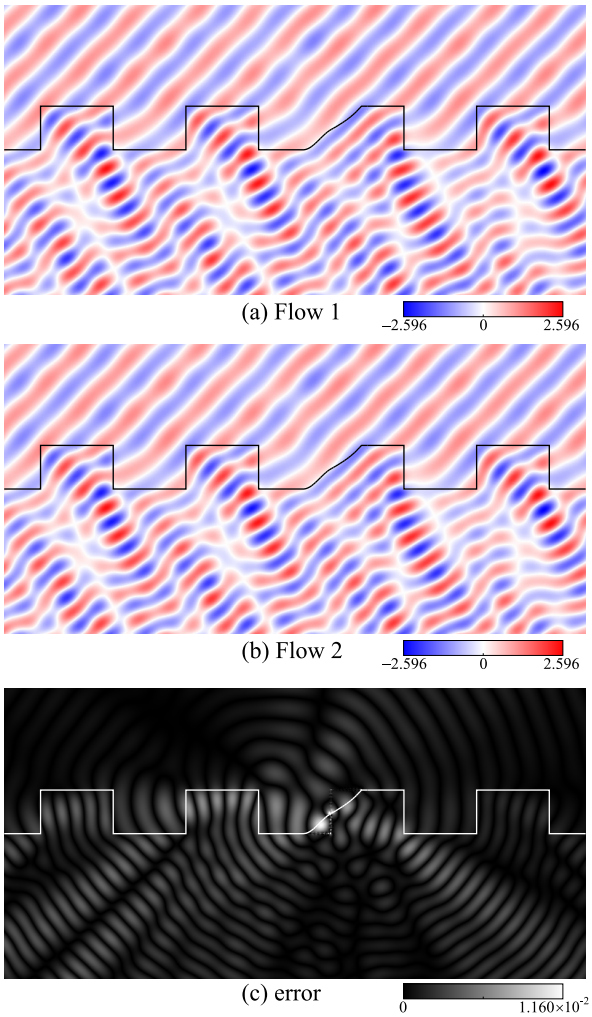


**Fig. 4** Total field distributions for the deformed-groove structure calculated by (a) Flow 1 [Fig. 3 (a)] and (a) Flow 2 [Fig. 3 (b)]. The error of these field distributions is plotted in (c).

Next, we evaluated the error at the far field for the deformed-groove grating between Flow 1 and Flow 2. The difference field at a long distance away from the defect is given by the integral expressions of the DFBEM by replacing the Green's function with its asymptotic form at far dis-

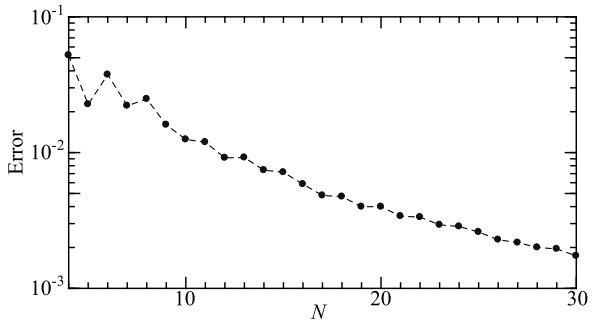


**Fig. 5** Convergence of the error in the total field at $(x, y) = (0.16T, 0.033T)$ between Flow 1 and Flow 2. The lengths of the boundary elements are set so as to be less than $\lambda/N$.

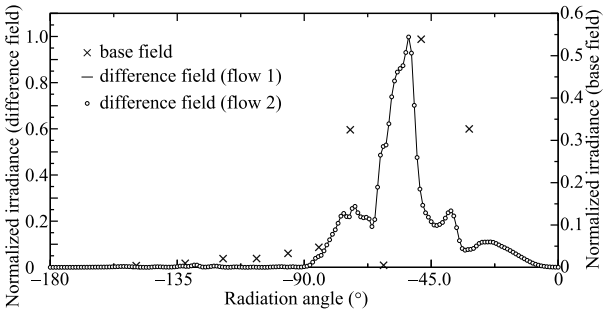


**Fig. 6** The far-field distribution for the deformed-groove structure in Fig. 1 (b). The base-field component [far field for Fig. 1 (a)] (cross marks) was defined by the amplitude of diffracted plane waves normalized by that of the incident wave. The difference-field components [the difference in the far fields between Fig. 1 (a) and 1 (b)] (solid lines for Flow 1 and open circles for Flow 2) were computed by the integral expressions of DFBEM, and normalized by the maximum value in the result for Flow 1.

tance. The far field obtained by the asymptotic form of the Green's function becomes a function of the direction from the defect. We computed the far field of the transmission side ($S_{10}$) with angles from $-180°$ to $0°$ in $1°$ increments. The total field for the deformed grating in $S_{10}$ is expressed as $f_1^{(2)} + \Delta f_1^{(2)} = f_1^{(1)} + \Delta f_1^{(1)} + \Delta f_1^{(2)}$. The difference-field components, $\Delta f_1^{(1)} + \Delta f_1^{(2)}$, for Flow 1 and Flow 2 are plotted in Fig. 6 with solid lines and open circles, respectively. They are normalized by the maximum of the difference field for Flow 1. The base-field component, $f_1^{(1)}$ corresponds to the plane waves diffracted from the original periodic grating. These amplitude normalized by that of the incident wave is plotted in Fig. 6 with cross marks. The base-field component and difference-field component were plotted separately because the base field is defined by the amplitude of the diffracted plane wave, whereas the difference-field component is defined by the integral expression. The difference fields obtained by Flow 1 and Flow 2 were very close. We found the maximum error at $-50°$, which is 0.348% of the maximum irradiance of the difference field at $-53°$. This relative error is as small as that in the field distribution around the defect.

Finally we validated the proposed DFBEM algorithm by comparing with the standard BEM. The standard BEM

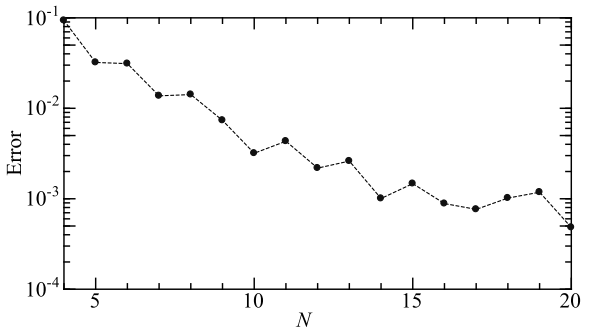


**Fig. 7** Convergence of the error in the total field (absolute of the difference in two complex values) at $(x, y) = (0.16T, 0.033T)$ between DFBEM (Flow 1) and the standard BEM. The lengths of the boundary elements are set so as to be less than $\lambda/N$.

cannot be applied to the deformed grating [Fig. 1 (b)] with a plane-wave incidence because infinitely long path integral along the grating surface is necessary. Thus, we reduced the width of the incident wave with a window function [8]:

$$g(x) = \begin{cases} 1, & (0 \le |x| < \frac{W}{2}), \\ \cos^2\left[\frac{|x|-W/2}{2(D-W)}\pi\right], & (\frac{W}{2} \le |x| < D - \frac{W}{2}), \\ 0, & (D - \frac{W}{2} \le |x|), \end{cases} \tag{4}$$

where $D = 18T$ and $W = 16T$. We assumed that the fields on the integral paths $C_{01}$ ($x \le -10.5T$) and $C_{02}$ ($10.5T \le x$) are zero, and therefore truncated those integral paths at $x = \pm 10.5T$. Refractive indices in $S_{10}$, $S_{31}$, $S_{20}$, $S_{32}$ were set to 1.5, 1.5, 1.0, and 1.0, respectively.

Calculation by DFBEM for comparison was also performed with the plane wave truncated by $g(x)$ and integral paths truncated at $x = \pm 10.5T$ for both the base field and the difference field. The base field is given by setting the refractive indices in $S_{10}$, $S_{31}$, $S_{20}$, $S_{32}$ to 1.5, 1.0, 1.0, and 1.5. After that, the defects were added in the sequence of Flow 1.

The convergence of the total field at the observation point $(x, y) = (0.16T, 0.033T)$ is plotted in Fig. 7. As the element length becomes shorter, the error between DFBEM and the standard BEM exponentially converged to zero.

## 3. Conclusion

For analyses of various defect structures in gratings, we have developed an algorithm with defect partitioning and the sequential application of a DFBEM for different defect patterns. The proposed algorithm was validated by the convergence of the error between solutions for two different defect-addition sequences, and by the convergence of that between the proposed algorithm and the standard BEM. Therefore, DFBEM provides a unique solution not depending on the defect-addition sequence, and also provides a rigorous solution that satisfies the wave equation and boundary conditions on dielectric interfaces as well as the standard BEM. In this demonstration, the sequential application of the DFBEM to the projection defect (to add a dielectric to the grating surface) and the DFBEM to the crack defect (to remove

a dielectric from the grating surface) enables us to freely deform the grating surface. In general, the defects can be partitioned into more than two sections, and the DFBEM can then be applied to each section. This process is helpful for expressing and analyzing complicated local defects such as buried grooves, rounded-edge grooves, local positional shifts in the grooves, rough grooves, mesa-structured grooves, and buried pillars on deformed grooves.

**References**

[1] C.M. Wang, H.I. Huang, C.C. Chao, J.Y. Chang, and Y. Sheng, "Transmission enhancement through a trench surrounded nano metallic slit by bump reflectors," Opt. Lett., vol.15, no.6, pp.3496–3501, March 2007.

[2] K. Watanabe, J. Pištora, and Y. Nakatake, "Rigorous coupled-wave analysis of electromagnetic scattering from lamellar grating with defects," Opt. Express, vol.19, no.25, pp.25799–25811, Dec. 2011.

[3] N. Nguyen-Huu, M. Cada, and J. Pištora, "Imperfectly geometric shapes of nanograting structures as solar absorbers with superior performance for solar cells," Opt. Express, vol.22, no.S2, pp.A282–A294, Jan. 2014.

[4] K. Hattori, J. Nakayama, and Y. Tamura, "Scattering of TM plane wave from periodic grating with single defect," IEICE Trans. Electron, vol.E91-C, no.1, pp.17–25, Jan. 2008.

[5] K. Trotskovsky and Y. Leviatan, "Source-model technique analysis of electromagnetic scattering by surface grooves and slits," J. Opt. Soc. Am. A, vol.28, no.4, pp.502–510, March 2011.

[6] J.-I. Sugisaka, T. Yasui, and K. Hirayama, "Expansion of the difference-field boundary element method for numerical analyses of various local defects in periodic surface-relief structures," J. Opt. Soc. Am. A, vol.32, no.5, p.751, 2015.

[7] Y. Nakata and M. Koshiba, "Boundary-element analysis of plane-wave diffraction from groove-type dielectric and metallic gratings," J. Opt. Soc. Am. A, vol.7, no.8, pp.1494–1502, Aug. 1990.

[8] A.D. Papadopoulos and E.N. Glytsis, "Finite-difference-time-domain analysis of finite-number-of-periods holographic and surface-relief gratings," Appl. Opt, vol.47, no.12, pp.1981–1994, April 2008.